

Self-channeling of a powerful microwave beam in a preliminarily formed plasma

Y. Cao, J. G. Leopold, Y. P. Bliokh, and Ya. E. Krasik
 Physics Department, Technion, Haifa 32000, Israel

(Received 7 August 2018; accepted 4 September 2018; published online 2 October 2018)

The self-channeling of a high power (≤ 500 MW) sub-nanosecond microwave beam in the plasma formed by a neutral gas ($>10^3$ Pa) ionization was demonstrated by Shafir *et al.* [Phys. Rev. Lett. **120**, 135003 (2018)]. In the present research, this effect is observed and studied in detail in a plasma, preliminarily formed by an *rf* discharge, in a low (<150 Pa) pressure gas. The results of analytical modeling and numerical particle-in-cell simulations show that ionization-induced channeling can be realized at a significantly lower power of the microwave beam and gas pressure if the preliminarily formed plasma is radially non-uniform with minimal on axis density. *Published by AIP Publishing.* <https://doi.org/10.1063/1.5051226>

I. INTRODUCTION

The ionization-induced channeling (IIC) of an intense microwave (MW) beam propagating through neutral gas has been predicted theoretically¹ and observed experimentally more than 30 years later.^{2,3} *Electron impact ionization* of a neutral gas in strong electromagnetic field is responsible for IIC. Other mechanisms are responsible for self-focusing a beam of an intense electromagnetic radiation in a *preliminarily prepared* plasma.^{4–8} It is important to note that the ponderomotive force, which plays a crucial role in the self-focusing of an intense laser beam propagating through plasma, cannot be responsible for the self-guiding phenomenon of a microwave (MW) beam with the parameters, considered in this paper: frequency $f \approx 10$ GHz, power density of ~ 1 GW/cm², radius of ~ 1.5 cm, and pulse duration less than 1 ns. The ponderomotive force $F = -\frac{e^2}{4m(2\pi f)^2} \nabla(E^2)$ of this beam needs a considerably longer time (~ 10 ns) than the MW pulse duration to be able to shift electrons to a distance larger than the beam radius and, therefore it cannot be responsible for the redistribution of the plasma density to form a channel.

In neutral gas, when the energy of background electrons oscillating in the electric field of the microwave beam exceeds significantly the impact ionization energy, then the ionization rate and, consequently, the density of the generated plasma are larger at the periphery of a bell-shaped (e.g., Gaussian) beam than on its axis. The resulting plasma “waveguide” traps part of the beam and suppresses significantly its diffraction divergence. IIC occurs for specific conditions only, i.e., the electric field is required to be above a threshold value; the pulse duration should be consistent with the gas pressure and seed electron density. These required conditions were defined in a theoretical model in Ref. 3, and experimentally verified^{2,3} for the case of high power microwave interaction with neutral gas at pressures $>10^3$ Pa.

In this paper, after eliminating some of the uncertainties in our earlier experiments^{2,3} which allow for more reproducibility, we report ionization induced self-channeling in a preliminarily formed and characterized plasma, of a short-duration microwave beam for even smaller power.

II. EXPERIMENTAL SETUP AND DIAGNOSTICS

In this research, the same experimental setup as that described in detail in Refs. 2 and 3, was used (see Fig. 1). A high-voltage (HV) generator based on magnetic compression stages and semiconductor opening switches⁹ produces a ~ 6 ns long pulse with a negative amplitude of ~ 320 kV and a rise time of ~ 0.5 ns on a matched 200Ω load. This pulse, applied on the sharp edge of the carbon cathode of the diode, generates explosive emission plasma¹⁰ serving as a source for a ~ 1.5 kA hollow (0.5 mm diameter) electron beam with electron energies up to ~ 270 keV.^{11–13} The electron beam is guided through the slow-wave structure (SWS) (3.2 cm inner diameter) by a 2.5 T magnetic field. Interaction of the beam with a synchronous backward TM₀₁ mode produces a 0.6 ns at FWHM (Full Width Half Maximum) microwave pulse (9.6 GHz). In order to obtain reproducible microwave beam generation, the cathode radius was reduced in comparison to the cathode described in Refs. 2 and 3, resulting in a lower microwave power of ≤ 300 MW. Passing through a mode converter and horn antenna, the linearly polarized microwave beam with a ~ 2.7 cm FWHM at the distance of ~ 9 cm from the antenna output aperture is irradiated towards an Ultem lens. The Ultem lens (focal length of ~ 9 cm) was placed inside the 100 cm long Pyrex tube with 24 cm inner diameter. At the focal plane, the microwave beam radius was ~ 1.6 cm corresponding to a Rayleigh length of 5.4 cm and an electric field of ≤ 135 kV/cm.

The applied voltage and diode current waveforms were measured using a capacitive voltage divider and a self-integrated Rogowski coil, respectively. In these experiments, the waveform of the microwaves at the output of the mode converter was measured by a directional coupler.¹⁴ The waveforms of the transmitted and scattered microwaves were measured by standard WR 10 dB receiving and side antennas (see Fig. 1).

A preliminary plasma was generated inside the Pyrex tube by a 2 MHz inductively coupled ~ 300 ms long *rf* discharge, induced by a quadrupole antenna in either He or Ar within a range of 5–130 Pa gas pressure. The parameters of the *rf* plasma were studied earlier¹⁵ without the presence of

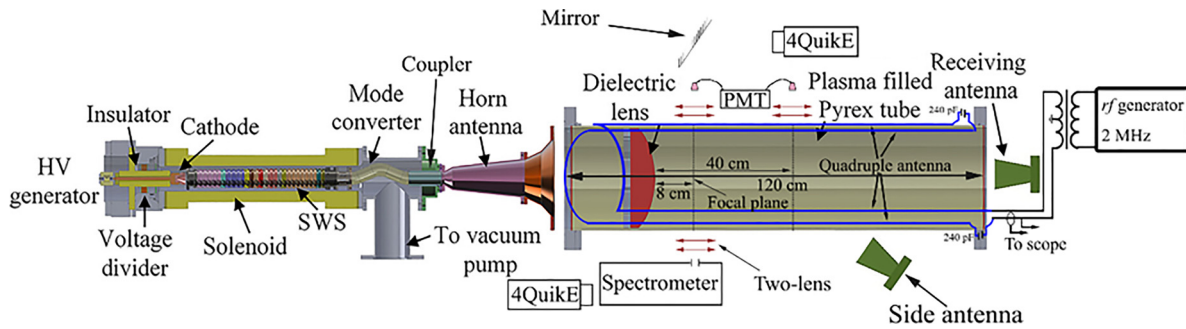


FIG. 1. Schematic drawing of the experimental setup, including the microwave generator, antenna, dielectric lens, and the glass filled Pyrex tube. The various diagnostic probes are also sketched. Note, the *rf* generator and the quadrupole antennas located on the walls of the Pyrex tube.

the Ultem lens inside the Pyrex tube. In the present work, we used microwave interferometry and visible spectroscopy to determine the plasma parameters along a line extending from the tip of the lens and averaged along 240 mm in the radial direction. For spectroscopic measurements, we used a Chromex 250i spectrometer (1800 grooves/mm grating, spectral resolution of ~ 0.03 nm/pixel) with a 4QuikE intensified camera (Stanford Computer Optics) at its output. The 4QuikE camera was also applied to record images of the plasma light emission prior and after the microwave beam propagation. Two Hamamatsu H10721 photomultiplier tubes (PMT) with collimators were placed at different distances with respect to the Ultem lens (see Fig. 1) to obtain the temporal evolution of the plasma light emission intensity.

The gas flow was fed into the tube through a hole at the lens periphery. To determine the gas pressure prior to the *rf* discharge, an Edwards active thermocouple ATC-E gauge was placed inside the Pyrex tube at different distances along the tube. The data obtained by this gauge were corrected for He and Ar gases following Ref. 16. The background pressures of 10^{-3} Pa in the SWS and the electron diode, and $\sim 10^{-2}$ Pa in the Pyrex tube prior to He or Ar gas filling, were kept by scroll and turbo-molecular pumps.

III. EXPERIMENTAL RESULTS

A. Initial plasma diagnostics

Reliable ignition of the *rf* plasma discharge was obtained in the range of 0.4–1.2 kW *rf* power at ~ 50 Pa He and ~ 1.5 Pa Ar. Here, let us note that actual pressure of gas at the time of the microwave beam injection could be several times larger due to desorption of neutrals from tube and lens walls. For instance, the Edwards vacuum gauge placed outside of the Pyrex tube exit showed increase in pressure 2–3 times when the *rf* discharge is ignited. Nevertheless, further in the text, we will use values of pressure measured prior to the *rf* discharge because of uncertainty in data regarding time response of this vacuum gauge.

In the absence of the Ultem lens, the axial and radial distributions of the plasma density was found to be close to uniform.¹⁵ The lens can change these distributions at the distances comparable with the lens radius because of the change of *rf* field configuration and absorption/desorption processes at the lens surface. With the lens, the radially averaged density measured by microwave interferometry, increases gradually along

the axis, as it is shown in Fig. 2. Similar axial distribution of the plasma density was obtained for Ar plasma at ~ 1.5 Pa. The errors in the plasma density measurements at the distances $z = 9$ cm, 25 cm, and 40 cm (henceforward, the distances along the tube axis, z , are measured from the lens tip, $z = 0$), were $\pm 10^{10}$ cm $^{-3}$, $\pm 3 \times 10^{10}$ cm $^{-3}$, and $\pm 4 \times 10^{10}$ cm $^{-3}$, respectively. Moreover, one can see that at $z = 9$ cm, the plasma density increases with increasing *rf* power less than at larger distances. This can be related to the increase in neutral gas density due to desorption from the lens surface induced by plasma ion bombardment, which causes a decrease in the electron temperature near the lens surface.

Spectroscopic measurements of emission of H_α and H_β spectral lines of excited hydrogen atoms desorbed from the lens surface confirm this assumption. Intensity ratio of these spectral lines, I_α and I_β , was used to estimate plasma electron temperatures at different axial positions considering the corona approximation which is valid for low-density plasma and Boltzmann distribution of the excited 3rd and 4th energy levels population. The plasma electron temperature was estimated as $kT_e = (E_{42} - E_{32}) [\ln(\frac{I_\alpha}{I_\beta} \cdot \frac{g_4 A_{42}}{g_3 A_{32}} \frac{\lambda_\alpha}{\lambda_\beta})]^{-1}$, where λ_{im} is the wavelength for the $i - m$ transition, where i designates the upper level, g_i is the degeneracy, A_{im} is the transition probability for spontaneous radiative emission from the level i to the lower level m , and E_i is the energy of level i . These estimates show that at $z = 9$ cm, the electron temperature is 0.57 ± 0.3 eV, which is smaller than at $z = 40$ cm, where the

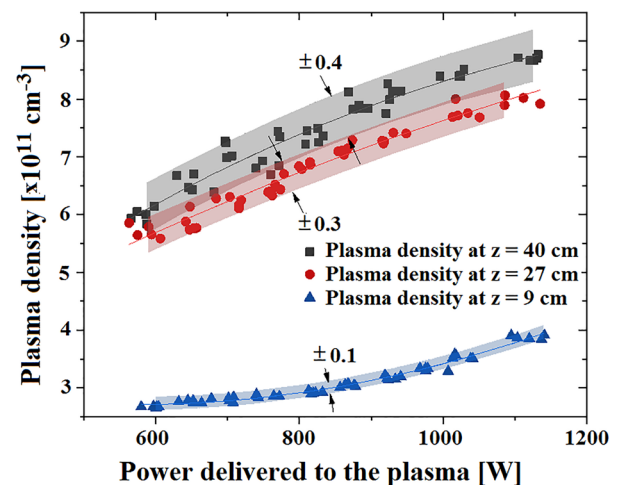


FIG. 2. Average plasma density vs. the *rf* power measured at different axial distances from the tip of the Ultem lens at $z = 0$ for ~ 50 Pa neutral He.

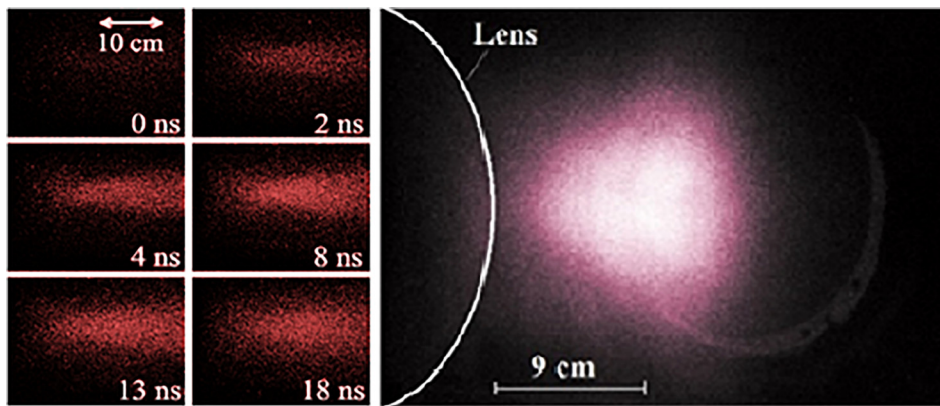


FIG. 3. (Left) Fast framing images of Ar plasma light emission after the microwave beam propagation in preliminary plasma (gas pressure of ~ 1.5 Pa) with preliminary density of $\sim 7 \times 10^{10} \text{ cm}^{-3}$. 0 ns corresponds to the microwave beam entrance time at $z=0$ (tip of the lens). (Right) Fast framing image (frame of 10 ns) of the plasma light emission at $t=10$ ns and gas pressure of ~ 20 Pa.

temperature is 0.67 ± 0.2 eV. The latter agrees with electron cooling by collisions with neutral which density can be larger at smaller distances to the lens tip. Thus, one can assume that the presence of the parabolic lens leads to a non-uniform radial distribution of the plasma density at the focal plane.

B. Plasma created by the microwave pulse

Images of the Ar plasma light emission (frame duration of 1.2 ns) after the microwave beam propagation are shown in Fig. 3 (left panels). One can see a well-defined, more than 30 cm long, radially confined (~ 5 cm in diameter) plasma column formation, 6 times longer than the Rayleigh length for beam propagation in vacuum. Similar images were obtained for He plasma at a gas pressure of ~ 50 Pa and rf plasma density of $\sim 2.6 \times 10^{11} \text{ cm}^{-3}$ at the focal plane of the lens. Formation of this narrow plasma channel suggests self-channeling of the microwave beam similar to those obtained in earlier research.^{2,3} It is worth to note that the self-channeling was observed only within the density ranges of $(2-3) \times 10^{11} \text{ cm}^{-3}$ and $(1.5-5) \times 10^{11} \text{ cm}^{-3}$ for He and Ar rf plasmas, respectively. At larger rf plasma densities, a sharp cut-off of the plasma channel at $z=13$ cm was observed (see Fig. 3, right panel). For smaller rf plasma densities, the light emission was too small for visual observation of the channel.

C. Microwave diagnostics

Microwave signals, propagating through the tube and scattered in the region near the focal plane, are registered by the front and side antennas, correspondingly (see Fig. 1). The front antenna is placed at the axis at the distance of

140 cm from the lens tip. The side antenna is placed at an angle of 135° (antenna is directed to the focal region) at 35 cm from the axis and 80 cm from the lens tip. The amplitude and waveform of the power of these signals depend on density of the preliminary formed He plasma, as it is shown in Figs. 4(a) and 4(b). The total energies received by the antennas at different initial plasma densities (area under corresponding curve in Fig. 4) are shown in Fig. 5. Similar results were obtained for Ar plasma at a gas pressure of 1.5 Pa.

Let us analyze the presented results. One can see that the waveform of the scattered microwave power (side antenna signal) is almost independent of the preliminary plasma density [Fig. 4(a)] and is the same as the waveform of the power signal registered by the coupler. However, the amplitude of the scattered microwaves varies with the increase in the plasma density. The presence of the scattered microwaves without the plasma [curve “A” in Fig. 4(a)] means that possible sources of these signals are scattering at the tube surface, diffraction at the lens edges, etc.

At the initial plasma density $n_p \approx 2.2 \times 10^{11} \text{ cm}^{-3}$, the scattered field amplitude [compare curves “A” and “B” in Fig. 4(a)] and integrated energy (see Fig. 5) increase and exceed the ones corresponding to $n_p = 0$. Simultaneously, the transmitted signal is weakened considerably. The reason is the plasma, created by microwave pulse at the focal plane of the lens. This plasma enhances the microwave scattering and decreases the transmitted signal.

As the initial plasma density increases, the ionization-induced microwave energy loss increases also. The scattered signal decreases gradually holding its shape [curves “C” and “D” in Fig. 4(a)]. In regard to the transmitted signal, initially

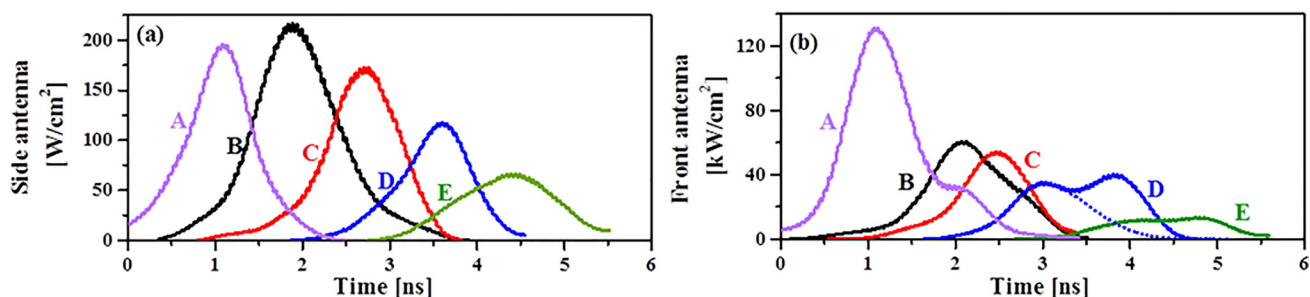


FIG. 4. Microwave energy fluxes registered by the side (a) and front (b) antennas for different initial plasma densities n_p and He pressure of 50 Pa. Curves marked by A correspond to vacuum, B— $n_p = 2.2 \times 10^{11} \text{ cm}^{-3}$, C— $n_p = 2.4 \times 10^{11} \text{ cm}^{-3}$, D— $n_p = 2.7 \times 10^{11} \text{ cm}^{-3}$, and E— $n_p = 3 \times 10^{11} \text{ cm}^{-3}$.

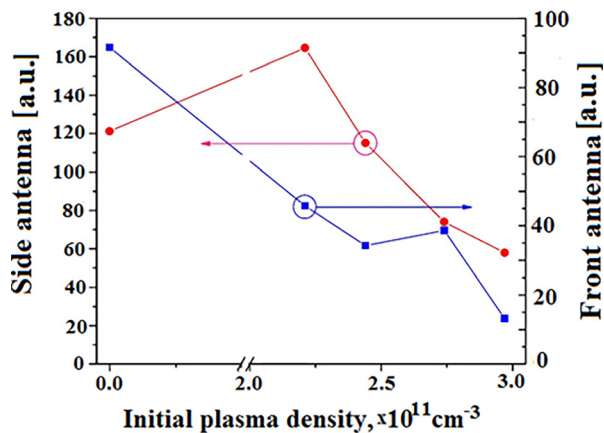


FIG. 5. The total energy (in arbitrary units) received by the side (left scale) and front (right scale) antennas as a function of the initial plasma density.

it also holds its shape and decreases its intensity [curve “C” in Fig. 4(b)]. However, further increase in the initial plasma density leads to strong deformation of the pulse shape: a dip appears in the middle of the pulse. Simultaneously, the total energy, transmitted to the front antenna, increases appreciably (see Fig. 5), which can be explained by the hollow plasma channel formation in the focal region. This channel traps essential cross-section of the microwave beam, reduces the beam divergence, and, as a result, increases the power delivered to the front antenna. One can consider that without the channel formation, the trailing edge of the pulse might be expected to appear as it is shown in Fig. 4(b) by dashed line (curve “D”). The absolute values of the transmitted microwave power measured by the receiving antenna versus the initial plasma density are shown in Fig. 6. One can see clearly increase in the transmitted power at initial plasma density of $2.8 \pm 0.1 \text{ cm}^{-3}$.

At a rather large density of the initial plasma, ionization-induced dissipation and scattering of the transmitted signal are heavily attenuated and its shape is blurred [see curve “E” in Fig. 4(b)].

D. Plasma light emission

For Ar plasma, in Fig. 7(a), the plasma light emission intensity measured by the collimated PMTs (see Fig. 1) at

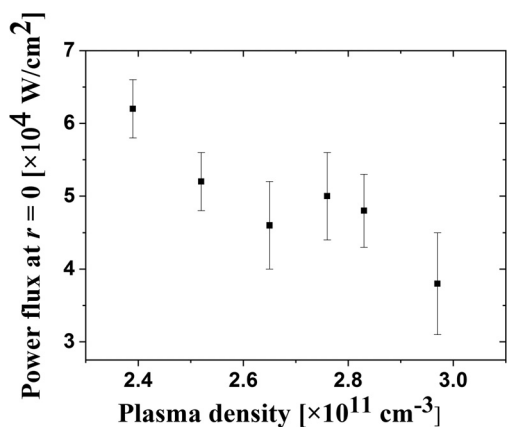


FIG. 6. Transmitted microwave power density measured on the axis ($r=0 \text{ cm}$) and $z=140 \text{ cm}$ vs. preliminary plasma density for 50 Pa neutral He.

$z=40 \text{ cm}$ and at the lens focal position at $z=9 \text{ cm}$ prior and after the microwave beam propagation is presented. One can see that microwave beam interaction with plasma leads to expected sharp increase in the plasma light emission intensity due to increased energy and density of the plasma electrons.^{2,3} This increased light emission decays to its initial level within several hundreds of nanoseconds. The ratio between the peaks in the plasma light intensities measured at $z=40 \text{ cm}$ and $z=9 \text{ cm}$ [see Fig. 7(b)] shows increase with the increase in the density of the preliminary plasma. The latter can be associated with a larger power of the beam at $z=40 \text{ cm}$ at increased density of the preliminary plasma, manifesting a self-guiding effect.

Spectroscopic measurements of H_α and H_β spectral line intensities were carried out with the 4QuikE camera frame duration of $40 \mu\text{s}$, prior, and 200 ns after the microwave beam interaction with the preliminary He plasma. The difference in the frame durations was related to necessity to observe reliable profiles of these spectral lines. After the normalization of the H_α and H_β spectral line intensities, i.e., accounting the difference in the frame time duration and camera magnification factors, it was found that intensity of these lines was increased ~ 5 times after the beam interaction with plasma. This significant increase in the H_α and H_β spectral line intensities is related to the increase in the electron temperature, and, respectively, plasma density.

IV. DISCUSSION

The ULTEM lens changes considerably the initial plasma density distribution $n_{pl0}(r) = n_{pl}(r, t=0)$ because of plasma ions recombination, absorption, neutral desorption, etc., which occur at the lens surface. These processes and the convexity of the lens surface can lead to the initial plasma density being smaller along the axis. This is a favorable initial condition for the formation of a two-humped plasma density profile as a result of microwave pulse interaction with such plasma even at smaller neutral density or MW power. The validity of this hypothesis will be verified below using a modified version of 1D model described in Refs. 2 and 3.

Let us model the radial distribution of the initial plasma density $n_{pl0}(r)$ in the focal plane as

$$n_{pl0}(r) = n_0 \cdot (1 - \Delta n \cdot e^{-r^2/\Delta r^2}), \quad (1)$$

where the parameters Δn and Δr characterize the depth and the width of the density dip near the axis.

To estimate the range of the plasma and microwave parameter values which allow the microwave beam’s self-channeling, let us consider instead of a smooth radial distribution of the plasma density across the channel, a step-like one. Namely, let us associate the plasma density n_1 at the axis (local minimum of the density) with the core plasma density, and the density n_2 , $n_2 > n_1$, of the local maximum (if it exists) at the microwave beam periphery, as a channel wall plasma density. Such a “hollow” plasma channel can trap a microwave beam, just like an optical fiber. Then, the difference between the reflection coefficients of the channel core and wall becomes sufficient for total internal reflection

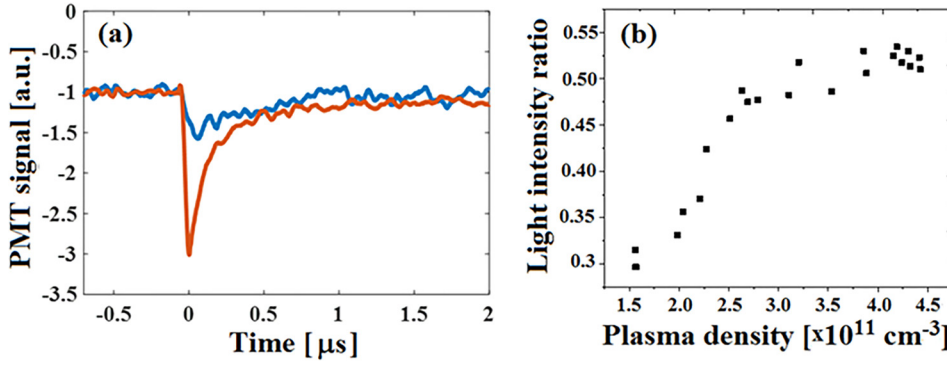


FIG. 7. (a) Light emission from the plasma obtained at $z=40$ cm (blue) and $z=9$ cm (red) for preliminary Ar plasma of $4.4 \times 10^{11} \text{ cm}^{-3}$. (b) Dependence of the plasma light intensities ratio obtained at $z=40$ and $z=9$ cm vs. the density of the preliminary plasma density. Zero time corresponds to the microwave beam propagation through the plasma.

(TIR) of the focused microwave beam. The angle of divergence of the Gaussian beam, φ , can be estimated as $\varphi \cong \lambda/\pi r_{beam}$, where λ is the microwave wavelength, and r_{beam} is the beam waist radius at the focal plane. The beam will be trapped into the channel when the angle of incidence θ at the interface between the channel core and the wall exceeds the critical value θ_{TIR} , defined as

$$\sin^2 \theta_{TIR} = \frac{1 - n_2/n_{crit}}{1 - n_1/n_{crit}}. \quad (2)$$

Here, $n_{1,2}$ are the plasma densities at the axis and at the channel wall, respectively, and n_{crit} is the critical plasma density. Using the beam parameter values $\lambda \cong 3$ cm and $r_{beam} \cong 2 - 3$ cm, φ can be estimated as $\varphi \cong 0.32$ (the value $r_{beam} = 3$ cm will be used hereafter for definiteness). The angle of divergence φ and the angle of incidence are related as $\varphi + \theta = \pi/2$, so that the TIR condition can be written as

$$\cos^2 \varphi = \sin^2 \theta \geq \sin^2 \theta_{TIR} = \frac{1 - n_2/n_{crit}}{1 - n_1/n_{crit}}. \quad (3)$$

Let us present condition Eq. (3) as

$$\cos^2 \varphi \geq \frac{1 - \eta_2 \mu}{1 - \eta_1 \mu}, \quad (4)$$

where $\eta_{1,2} = n_{1,2}/n_0$, and $\mu = n_0/n_{crit}$ are the normalized plasma densities. The normalized plasma densities $\eta_{1,2}$ are the functions of time, $\eta_{1,2} = \eta_{1,2}(t)$, so that the condition in Eq. (4) can, in general, be satisfied during a limited period of the pulse duration.

The microwave propagation through the channel is possible until the core's plasma density is less than the critical value

$$n_1/n_{crit} = \eta_1 \mu \leq 1. \quad (5)$$

The two inequalities, Eqs. (4) and (5), define simultaneously the range of possible values of the initial plasma density and the time interval, when channeling occurs. Indeed, let us rewrite these inequalities as

$$\frac{\sin^2 \varphi}{\eta_2(t) - \eta_1(t) \cos^2 \varphi} \equiv \mu_{low}(t) \leq \mu \leq \mu_{high}(t) \equiv \frac{1}{\eta_1(t)}. \quad (6)$$

In the model considered, plasma densities on axis, $n_{pl}(r=0, t)$, and at the local maximum at the beam

periphery, $n_{pl}(r=r_{max}, t)$, are associated with the channel core and wall densities $\eta_{1,2}(t)$. The evolution of the electron density $n_{pl}(r, t)$ is described by the expression

$$n_{pl}(r, t) = n_{pl0}(r) \cdot \exp \left\{ n_g \int_{-\infty}^t dt' \sigma[w(t')] |v(t')| \right\}, \quad (7)$$

where n_g is the neutral gas density, $v(t)$ and $w(t)$ are the electron velocity and kinetic energy, respectively, and σ is the electron impact ionization cross-section. Detailed analysis of Eq. (7) as applied to short powerful microwave pulses is given in Ref. 3.

Using the solutions of Eq. (7) the relation between $\eta_{1,2}(t)$ and $n_{pl}(r, t)$, the conditions in Eq. (6) can be presented graphically as shown in Fig. 8.

The following values of the parameters were used: $\Delta n = 0.32$ [panel (a)] and $\Delta n = 0$ [panel (b)], $\Delta r = 1.3r_{beam}$, the neutral gas pressure $p = 150$ Pa, and maximal amplitude of the pulsed electric field $E_0 = 135$ kV/cm [panel (a)] and $E_0 = 300$ kV/cm [panel (b)]. The dashed lines correspond $n_0 = 2.75 \times 10^{11} \text{ cm}^{-3}$.

Figure 8(a) demonstrates that the channeling is sensitive to the initial plasma density, i.e., to the value of the parameter μ . There is an optimal value of the plasma density (optimal value of μ , marked by the dashed line), for which the pulse channeling is most effective. The channeling appears earlier and lasts shorter as the density (parameter μ) increases. The smaller value of μ shifts the channeling to the end of the pulse where the intensity is small. These non-optimal values of μ are shown by dotted lines in Fig. 8(a). One can see that for $n_0 = 2.75 \times 10^{11} \text{ cm}^{-3}$, the second half of the pulse is trapped in the channel. The latter agrees with the shape of the transmitted pulse ‘‘D’’ in Fig. 4. The comparison between Figs. 8(a) and 8(b) shows that in the initially homogeneous plasma, channeling occurs for much more powerful pulses.

In spite that the considered ‘‘plasma fiber’’ model is rather approximate, using parameters’ values which are close to the experimental ones, the model explains observed evolution of the transmitted pulses, presented in Fig. 4, under the initial plasma density variation. The assumed radial inhomogeneity of the initial plasma density is a likely reason for the channel formation by the microwave pulse with relatively low, about 130 kV/cm, electric field amplitude, whereas in the homogeneous plasma the pulse self-channeling requires much more strong, above 300 kV/cm, electric fields.

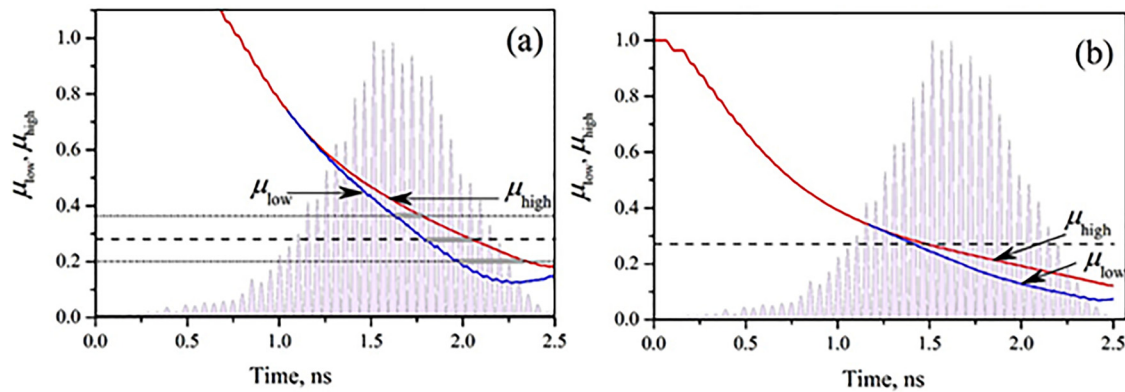


FIG. 8. Graphical representation of the inequalities Eq. (6). (a) Radially inhomogeneous distribution of the initial plasma density. (b) Homogeneous plasma density. The functions $\mu_{\text{low}}(t)$ and $\mu_{\text{high}}(t)$ are obtained as solutions of Eq. (7). The dashed horizontal lines correspond $n_0 = 2.75 \times 10^{11} \text{ cm}^{-3}$; the microwave pulse intensity, $I(t) \sim E^2(t)$, is shown by the gray shaded area. The microwave beam is trapped into the hollow plasma channel when a $\mu = \text{const}$ line is placed between curves $\mu_{\text{low}}(t)$ and $\mu_{\text{high}}(t)$ [gray rectangles in panel (a)].

To support the above theoretical model, we performed numerical simulations using the Lsp^{17–19} hybrid particle-in-cell (PIC) code. The collisional plasma is treated by Monte Carlo, whereas the electrodynamics by the PIC technique. The number of particles is restrained by a particle collapsing method which bundles together particles at the same location and same momentum. To avoid Debye heating, kinetic electrons can migrate to become fluid particles with fluid dynamics governing their motion. A Gaussian 135 kV/cm, 10 GHz MW beam with a rectangular leading front is injected into the interaction space and is focused numerically rather than by a dielectric lens. The tip of the dielectric lens tip is assumed to be at $z=0$ cm, the focal point is at $z=9$ cm, the region $z=0$ to 50 cm, and $x=-10$ to 10 cm of the 2D simulation space is filled with gas and plasma. The gas modeled is He for which electron impact ionization and four of the most important excitation reactions are accounted for, using cross section functions given by Ralchenko *et al.*²⁰ Only

electron dynamics is considered, whereas atoms and ions are stationary.

To confirm the 1D theoretical model described above, we chose the same conditions as those in Fig. 8. The 2D interaction region is filled with 150 Pa neutral He. We consider either a uniform $2.75 \times 10^{11} \text{ cm}^{-3}$ density plasma or a non-uniform preliminary plasma density which radial distribution at focus ($z=9$ cm) is given by Eq. (1). We chose $n_{\text{pl0}}(z)$ to increase linearly from $z=0$ cm according to the dependence given in Fig. 2. In addition, $n_{\text{pl0}}(x, z)$ changes with x as the convex shape of the experimental lens so that Δx fixed at focus (Δr in the analytical model) increases with increasing z from $z=0$. The resulting time dependence of the plasma density contours is seen in Fig. 9.

Note in Fig. 9 that the upper limit of the plasma density contours is chosen to be at or above the critical density. The formation of a plasma channel is clearly seen for the simulated non-uniform preliminary plasma in Figs. 9(a)–9(c).

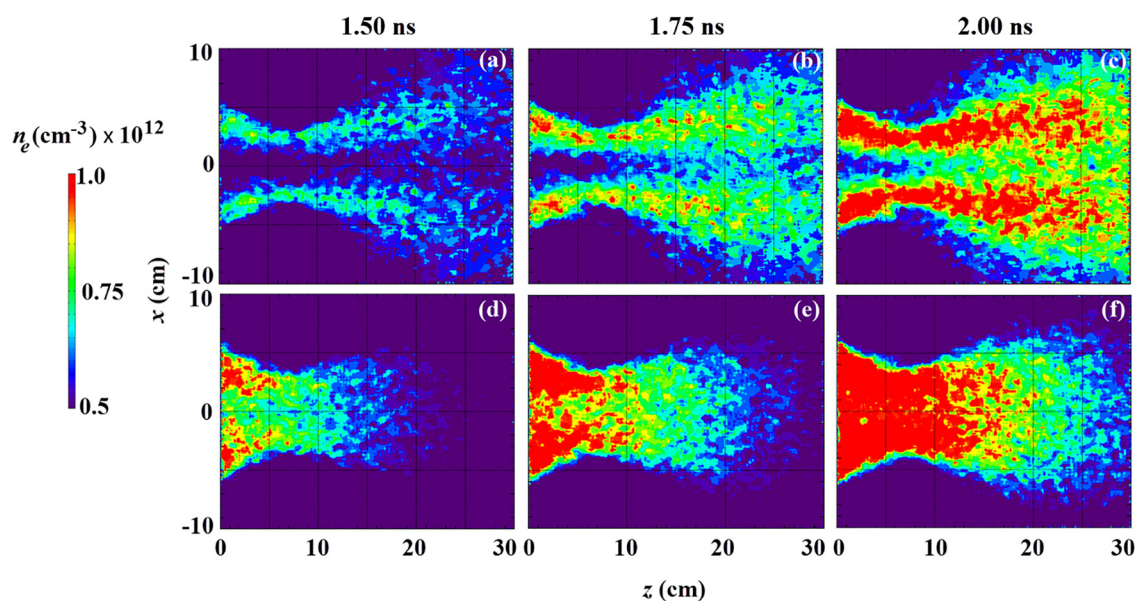


FIG. 9. Lsp simulated time and space resolved evolution of the He plasma electron density generated by the propagation of a 135 kV/cm, 10 GHz focused MW beam. Plasma density contours are drawn for a non-uniform (a)–(c) and a uniform (d)–(f) initial plasma distribution. $t = 1.50$ ns in (a) and (d), 1.75 ns in (b) and (e), and 2.00 ns in (c) and (f). Red is for $\geq 10^{12} \text{ cm}^{-3}$ and dark blue is for $\leq 5 \times 10^{11} \text{ cm}^{-3}$ plasma density.

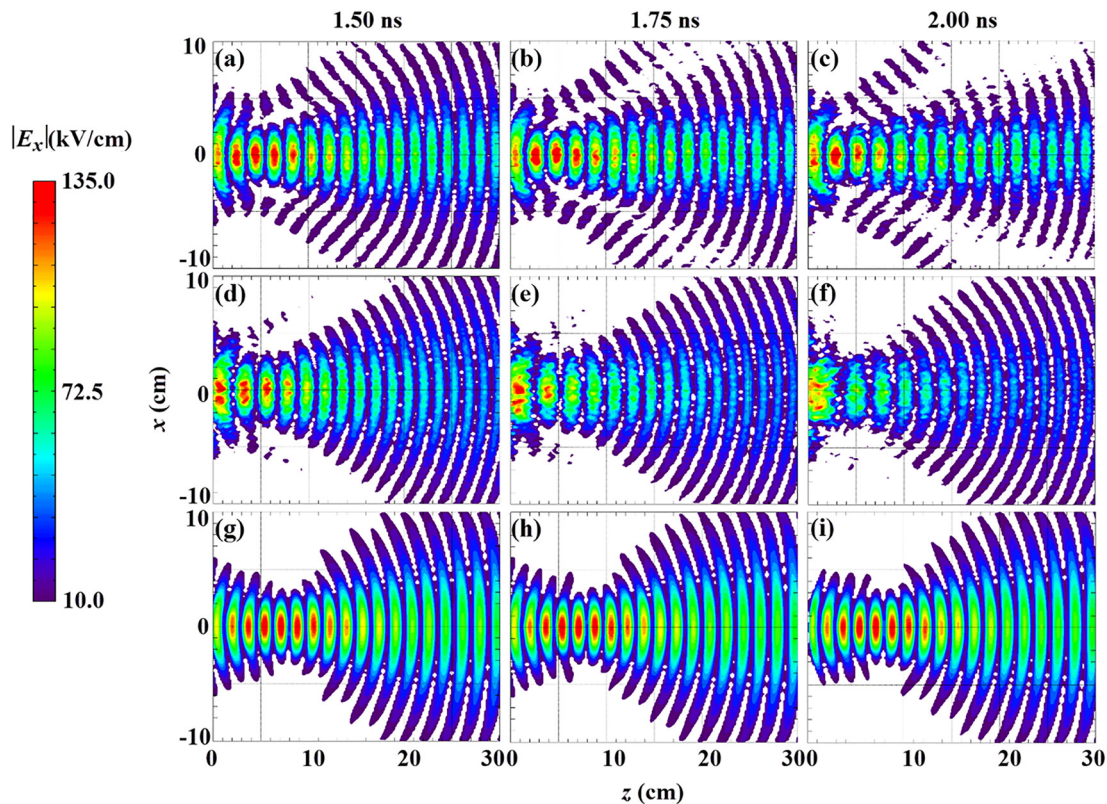


FIG. 10. Lsp simulated time and space resolved evolution of a 135 kV/cm, 10 GHz microwave focused beam. Absolute values of $|E_x|(z, x)$ are depicted at $t = 1.50$ ns (a), (d), and (g), 1.75 ns (b), (e), and (h), and 2.00 ns (c), (f), and (i). In (a)–(c), the preliminary plasma fill is non-uniform, in (d)–(f) the uniform, and in (g)–(i) a non-uniform plasma is present but no neutral gas or ionizations or excitations exist. The white background in these figures represents electric fields < 10 kV/cm.

When the preliminary plasma is uniform [Figs. 9(d)–9(f)], some channeling appears initially but the channel fills in quickly.

In Fig. 10, the propagation of the electric field component of the focused MW beam is drawn. In Figs. 10(a)–10(c), we clearly see the channeling of the MW field through the plasma channel [Figs. 9(a)–9(c)]. Moreover, scattering from the walls of the channel can also be depicted. These scattered fields have been observed in the experiment (Fig. 4). The simulated scattered beam changes its orientation as the plasma channel wall density and length increase. For a uniform preliminary plasma fill [Figs. 10(d)–10(f)], very little channeling appears and eventually the plasma density becomes critical around the axis. When this case is compared to Figs. 9(d)–9(f), we see that the ionization of the gas blocks the beam propagation rather than channeling it. For a uniform plasma, there is little beam scattering. In Figs. 10(g)–10(i), an initially non-uniform plasma fills the interaction region, but ionization or excitations are turned off. For this case, the MW beam crossing the region has no effect on the plasma, and the plasma does not perturb the beam. This means that ponderomotive forces have no role in the mechanism of the observed self-channeling.

V. SUMMARY

In this paper, the interaction of a high power (≤ 300 MW), sub-ns microwave beam with a preliminarily formed low density plasma and a low pressure neutral gas

is studied using microwave, optical, and spectroscopic methods. It is shown that ionization-induced self-channeling of the microwave beam occurs for much lower values of the wave amplitude when the density of the initial plasma is radially inhomogeneous. This experimental result is confirmed by an analytical model, describing the evolution of such a non-uniform plasma. PIC simulations support this model and confirm the experimental results. The model and the simulations confirm that the ionization of the neutral gas is responsible for the microwave beam's channeling.

ACKNOWLEDGMENTS

The authors are grateful to G. Shafir and D. Levko for fruitful discussions and to S. Gleizer and E. Flyat for technical assistance. This work was supported in part by the PAZY under Grant No. 2020960.

¹Y. L. Bogomolov, S. F. Lirin, V. E. Semenov, and A. M. Sergeev, *JETP Lett.* **45**, 532 (1987); available at <http://adsabs.harvard.edu/abs/1987ZhPmR..45..532B> and http://www.jetpletters.ac.ru/ps/1246/article_18849.pdf.

²G. Shafir, Y. E. Krasik, Y. P. Bliokh, D. Levko, Y. Cao, J. G. Leopold, R. Gad, V. Bernshtam, and A. Fisher, *Phys. Rev. Lett.* **120**, 135003 (2018).

³G. Shafir, Y. Cao, Y. Bliokh, J. G. Leopold, D. Levko, V. Rostov, R. Gad, A. Fisher, V. Bernshtam, and Y. E. Krasik, *Phys. Plasmas* **25**, 032308 (2018).

⁴Y. Tamaki, J. Itatani, Y. Nagata, M. Obara, and K. Midorikawa, *Phys. Rev. Lett.* **82**, 1422 (1999).

⁵G.-Z. Sun, E. Ott, Y. C. Lee, and P. Guzdar, *Phys. Fluids* **30**, 526 (1987).

⁶D. J. Spence, A. Butler, and S. M. Hooker, *J. Opt. Soc. Am. B* **20**, 138 (2003).

- ⁷P. Sprangle, C. M. Tang, and E. Esarey, *IEEE Trans. Plasma Sci.* **15**, 145 (1987).
- ⁸F. W. Perkins and E. J. Valeo, *Phys. Rev. Lett.* **32**, 1234 (1974).
- ⁹S. N. Rukin, *Instrum. Exp. Tech.* **42**(4), 439 (1999).
- ¹⁰G. A. Mesyats, *Explos. Electron Emission* (URO, Ekaterinburg, 1998).
- ¹¹G. Shafir, M. Kreif, J. Z. Gleizer, S. Gleizer, Y. E. Krasik, A. V. Gunin, O. P. Kutenkov, I. V. Pegel, and V. V. Rostov, *J. Appl. Phys.* **118**, 193302 (2015).
- ¹²N. S. Ginzburg, N. Y. Novozhilova, I. V. Zotova, A. S. Sergeev, N. Y. Peskov, A. D. Phelps, S. M. Wiggins, A. W. Cross, K. Ronald, W. He, V. G. Shpak, M. I. Yalandin, S. A. Shunailov, M. R. Ulmaskulov, and V. P. Tarakanov, *Phys. Rev. E: Stat. Phys., Plasmas, Fluids, Relat. Interdiscip. Top.* **60**, 3297 (1999).
- ¹³N. S. Ginzburg, I. V. Zotova, I. V. Pegel, V. V. Rostov, V. G. Shpak, and M. I. Yalandin, *Radiophys. Quantum Electron.* **50**, 762 (2007).
- ¹⁴L. M. Earley and W. P. Ballard, *IEEE Trans. Nucl. Sci.* **32**, 2921 (1985).
- ¹⁵G. Shafir, D. Zolotukhin, V. Godyak, A. Shlapakovski, S. Gleizer, Y. Slutsker, R. Gad, V. Bernshtam, Y. Ralchenko, and Y. E. Krasik, *Plasma Sources Sci. Technol.* **26**, 025005 (2017).
- ¹⁶R. Grinham and A. Chew, "Gas corrections factors for vacuum pressure gauges," *Vakuum* **29**, 25 (2017).
- ¹⁷D. R. Welch, D. V. Rose, B. V. Oliver, and R. E. Clark, *Nucl. Instrum. Methods Phys. Res., Sect. A* **464**, 134 (2001).
- ¹⁸C. Thoma, T. P. Hughes, N. L. Bruner, T. C. Genoni, D. R. Welch, and R. E. Clark, *IEEE Trans. Plasma Sci.* **34**, 910 (2006).
- ¹⁹D. V. Rose, D. R. Welch, R. E. Clark, C. Thoma, W. R. Zimmerman, N. Bruner, P. K. Rambo, and B. W. Atherton, *Phys. Plasmas* **18**, 093501 (2011).
- ²⁰Y. Ralchenko, R. K. Janev, T. Kato, D. V. Fursa, I. Bray, and F. J. de Heer, *At. Data Nucl. Data Tables* **94**, 603 (2008).